Estimation of neutron-equivalent dose in organs of patients undergoing radiotherapy by the use of a novel online digital detector

2012 Phys. Med. Biol. 57 6167

(http://iopscience.iop.org/0031-9155/57/19/6167)

IOP PUBLISHING PHYSICS IN MEDICINE AND BIOLOGY

Phys. Med. Biol. **57** (2012) 6167–6191 doi:10.1088/0031-9155/57/19/6167

Estimation of neutron-equivalent dose in organs of patients undergoing radiotherapy by the use of a novel online digital detector

F Sánchez-Doblado[1,2], C Domingo[3], F Gómez[4], B Sánchez-Nieto[5], J L Muñiz[6], M J García-Fusté[3], M R Expósito[2], R Barquero[7], G Hartmann[8], J A Terrón[1], J Pena[4], R Méndez[6], F Gutiérrez[9], F X Guerre[10], J Roselló[11], L Núñez[12], L Brualla-González[11], F Manchado[2], A Lorente[13], E Gallego[13], R Capote[14], D Planes[11], J I Lagares[6], X González-Soto[4], F Sansaloni[6], R Colmenares[15], K Amgarou[3], E Morales[3], R Bedogni[16], J P Cano[2] and F Fernández[17]

[1] Servicio de Radiofísica, Hospital Universitario Virgen Macarena, Sevilla, Spain
[2] Departamento de Fisiología Médica y Biofísica, Universidad de Sevilla, Sevilla, Spain
[3] Departamento de Física, Universitat Autònoma de Barcelona, Barcelona, Spain
[4] Departamento de Física de Partículas, Universidad de Santiago de Compostela, Santiago de Compostela, Spain
[5] Departamento de Física, Pontificia Universidad Católica de Chile, Santiago, Chile
[6] Centro de Investigaciones Energéticas, Medioambientales y Tecnológicas (CIEMAT), Madrid, Spain
[7] Servicio de Protección Radiológica, Hospital Universitario Río Hortega, Valladolid, Spain
[8] Department of Medical Physics in Radiotherapy, Deutsches Krebsforschungszentrum (DKFZ), Heidelberg, Germany
[9] Optoelectronics & New Technologies Laboratory, Alter Technology, Sevilla, Spain
[10] Hirex Engineering, Ramonville S, Agne, France
[11] Unidad de Radioterapia Hospital General Universitario de Valencia, ERESA, Valencia, Spain
[12] Servicio de Radiofísica, Hospital Universitario Puerta de Hierro, Majadahonda, Spain
[13] Departamento de Ingeniería Nuclear, Universidad Politécnica Madrid, Madrid, Spain
[14] International Atomic Energy Agency (IAEA), Viena, Austria
[15] Unidad de Radiofísica Clínica, Hospital Universitario Ramón y Cajal, Madrid, Spain
[16] Laboratori Nazionali di Frascati, Istituto Nazionale di Fisica Nucleare (INFN), Italy
[17] Consejo de Seguridad Nuclear (CSN), Madrid, Spain

E-mail: paco@us.es

Received 7 May 2012, in final form 18 July 2012
Published 13 September 2012
Online at stacks.iop.org/PMB/57/6167

Abstract

Neutron peripheral contamination in patients undergoing high-energy photon radiotherapy is considered as a risk factor for secondary cancer induction. Organ-specific neutron-equivalent dose estimation is therefore essential for a reasonable assessment of these associated risks. This work aimed to develop a method to estimate neutron-equivalent doses in multiple organs of radiotherapy patients. The method involved the convolution, at 16 reference points in an anthropomorphic phantom, of the normalized Monte Carlo neutron fluence energy spectra with the kerma and energy-dependent radiation weighting factor. This was then scaled with the total neutron fluence measured with passive

detectors, at the same reference points, in order to obtain the equivalent doses in organs. The latter were correlated with the readings of a neutron digital detector located inside the treatment room during phantom irradiation. This digital detector, designed and developed by our group, integrates the thermal neutron fluence. The correlation model, applied to the digital detector readings during patient irradiation, enables the online estimation of neutron-equivalent doses in organs. The model takes into account the specific irradiation site, the field parameters (energy, field size, angle incidence, etc) and the installation (linac and bunker geometry). This method, which is suitable for routine clinical use, will help to systematically generate the dosimetric data essential for the improvement of current risk-estimation models.

1. Introduction

There is a growing concern about the risk of secondary radiation-induced tumours as a consequence of the radiotherapy treatments. The comprehensive review article by Xu *et al* (2008) details the principles, methods and unresolved issues related to this subject.

Both scattered and leakage photon radiations, as well as secondary neutrons, are responsible for the peripheral unwanted dose. An out-of-field photon-absorbed dose is typically larger than a neutron-absorbed dose (Bednarz *et al* 2009), but because of the radiation weighting factor (w_R), neutrons may be the dominant source of tissue damage from secondary radiation at some locations (Kry *et al* 2005).

Epidemiological risk assessments should evaluate the secondary cancer rate incidences in a cohort of patients in relation to their organ-specific equivalent doses. In this sense, dosimetric data, properly generated, are essential to establish a reasonable assessment of these associated risks. There are previous dosimetric studies devoted to assess neutron and photon contamination. Xu *et al* (2008) covered some of these major dosimetric studies.

Treatment planning procedures provide detailed dosimetric information on the volume covered by the CT scan. However, to our knowledge, no systematic dosimetry methodology for the quantification of neutron-equivalent doses in organs outside the planning volume has been proposed yet.

The aim of this work was to develop a methodology for the systematic estimation of neutron-equivalent doses in organs for patients undergoing high-energy (above 10 MV) external photon beam radiotherapy. A measurement- and Monte Carlo (MC)-based model is presented here as a general applicable method for the online estimation of equivalent dose in specific organs of radiotherapy patients. First, an appropriate active digital neutron detector, based on the relation existing between upsets in digital memories and thermal neutron fluence, was designed and developed (Gómez *et al* 2010). This detector overcomes the problems of current active (mainly saturation and photon sensitivity) and passive (with time-consuming and cumbersome readout procedures) detectors. Whole-body anthropomorphic phantom measurements, carried out with passive detectors, combined with a detailed MC model are correlated with the digital detector readings under a variety of conditions which potentially could affect secondary neutron radiation. The same methodology is applicable to any other neutron-sensitive detector after a specific calibration procedure.

Being able to systematically estimate and report the neutron-equivalent dose in peripheral organs, similarly to what treatment planning systems perform in the case of in-field organs, will constitute a step towards providing some of the essential data needed for a proper secondary

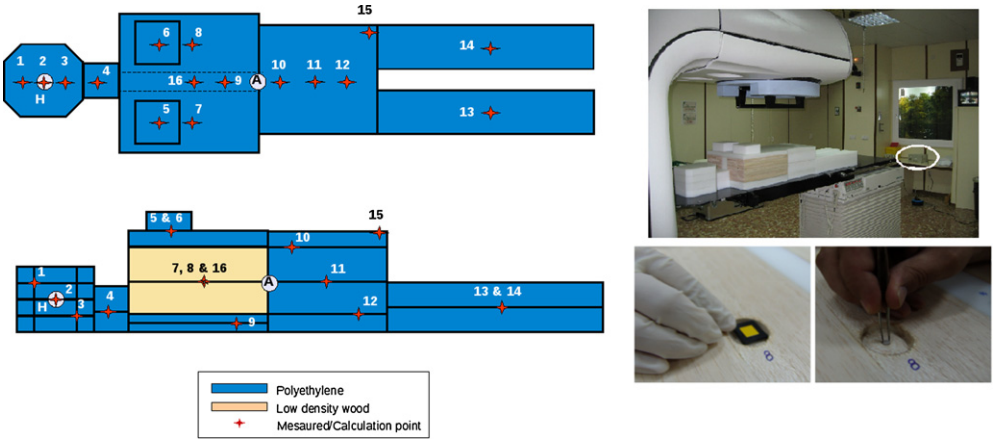

Figure 1. (Left) Scheme of the anthropomorphic phantom designed and built for this work (NORMA). It shows the points where measurements and simulations were performed. Points H and A represent the isocentres for head and abdomen treatments, respectively. (Top right) The phantom on the treatment couch and the digital detector located in the measurement position (circle) are shown. (Bottom right) Dedicated cavities inside NORMA to allocate the passive detectors are shown.

cancer risk analysis. The latter will be useful for a better treatment strategy selection. It will also be a valuable tool for comparing the relative level of secondary radiation for different accelerators and treatment procedures.

2. Material and methods

The purpose of this work entails establishing a methodology to correlate the readings of the active detector and the neutron-equivalent doses in pre-established specific organs of patients undergoing external photon beam radiotherapy.

First, a set of irradiation conditions which included single-beam incidences and complete radiotherapy treatments (see section 2.2) was defined. Second, a detailed model of the photoneutron field inside a radiotherapy treatment room and at specific points inside a whole-body anthropomorphic phantom was generated for the different irradiation conditions and treatment facilities chosen. This part of the study was performed by combining experimental neutron spectrometry with MC simulations. Third, fluence measurements were carried out for the defined irradiation setups. More specifically, simultaneous readings carried out with the digital detector inside the treatment room and with two types of passive detectors (poly-allyl-diglycol-carbonate (PADC) and ^{6}Li/^{7}Li thermoluminiscence dosimeters (TLD)) at specific points inside the anthropomorphic phantom were performed.

2.1. NORMA: the anthropomorphic phantom

A whole-body anthropomorphic female phantom called NORMA (figure 1) was designed and built—in polyethylene and low-density wood for lungs—with 16 measurement points distributed along it and covering different depths. The selection of the points in NORMA representing each organ was made using the organ sizes and positions from the revised version

Table 1. NORMA points to organs correlation.

Organs and tissues	NORMA points
Thyroid	4
Oesophagus	4, 9, 16
Lung	7, 8
Breast	5, 6, 15
Stomach	9, 11, 16
Liver	9, 10, 11, 16
Colon	11, 12
Urinary bladder	10
Ovary	11, 12
Skin	15
Bone	1, 3, 9, 12, 13, 14, 15
Bone marrow	9, 12, 15
Remainder	All except 7, 8, 15

of the Cristy anthropomorphic phantom (available at http://ordose.ornl.gov/resources/phantom). Table 1 shows the correspondence between organ and NORMA points. The authors are aware of the limitations of this methodology. However, doses inside the phantom do not show extremely sharp changes and the selected points could be accepted given our level of uncertainty. Nevertheless, extra measurements points were added in some organs to better simulate the different contributions to the dose (e.g., a skin point for breast). Thus, neutron-equivalent doses in organs were estimated through an average of the corresponding NORMA points.

2.2. Irradiation conditions

Seven different irradiation conditions were set up as follows:

(i) head and neck complete treatment, eight beam incidences (at 0°, 45°, 90°, 135°, 180°, 225°, 270°, 315°), 10 × 10 cm^2 field size, isocentre at point H (see figure 1),
(ii) abdomen complete treatment, the same beam incidences and field size as in *i*, isocentre at point A (see figure 1),
(iii) fixed 2 × 2 cm^2 irradiation field, gantry at 0°, isocentre at point A,
(iv) fixed 5 × 5 cm^2 irradiation field, gantry at 0°, isocentre at point A,
(v) fixed 20 × 20 cm^2 irradiation field, gantry at 0°, isocentre at point A,
(vi) fixed 10 × 10 cm^2 irradiation field, gantry at 0°, isocentre at point A,
(vii) fixed 10 × 10 cm^2 irradiation field, gantry at 270°, isocentre at point A.

All these irradiations were set to 1000 monitor units (MU).[18] The dose rate ranged from 300 to 600 MU min^{-1}. The used energy depends on the treatment facility.

For treatments (i) and (ii), dosimeters were placed at all 16 points in NORMA (see the inset of figure 1). The influence of the irradiation field size was studied from cases (iii) to (vi), with two measurement points (2 and 8) inside NORMA, while the influence of the beam entry angle was studied through cases (vi) and (vii), with six measurements points (2, 7, 8, 11, 13 and 14). Additionally, some real intensity-modulated radiotherapy therapy (IMRT) treatments were compared, from the point of view of neutron production, with cases (i) and (ii) using the same number of monitor units and gantry angles.

[18] One MU was calibrated to correspond to 1 cGy photon dose measured at the depth of maximum dose in water (source-to-surface distance equal to 100 cm).

Table 2. Description of irradiation facilities.

Facility	Linac	Nominal energy (MV)	Bunker volume (m^3)
Hospital Universitario Virgen Macarena (HUVM), Seville (Spain)[a]	Siemens Primus	15	317 (b1) 162 (b2)
Hospital Universitario Puerta de Hierro (HUPH), Majadahonda (Spain)	Varian Clinac 2100	15	205
Hospital Universitario Ramón y Cajal (HURC), Madrid (Spain)	Elekta Synergy	15	172
Hospital General Universitario de Valencia (HGUV), Valencia (Spain)	Siemens Primus	18	150
Universitäts Klinikum (UK), Heidelberg (Germany)	Siemens Mevatron	23	169

[a]At HUVM, two different bunkers (b1 and b2) with the same linac.

Irradiation facilities are described in table 2. In particular, the two linacs in Seville are of special interest in order to study bunker size dependence, as they are identical machines, operating under identical conditions, with the only difference being the treatment room volume: one of them considerably large (bunker 1: 317 m^3) and the other one considerably smaller (bunker 2: 162 m^3).

2.3. Neutron spectra MC simulations

The MC simulation was carried out using the MCNPX-2.6.0 code (Hendricks *et al* 2008) and following the detailed model of a Siemens PRIMUS and code libraries described by Pena *et al* (2005). More details about these simulations were given by Gónzalez-Soto *et al* (2012).

In order to take into account the fact that the amount of neutrons produced per MU depends appreciably on the energy of the primary electron beam, a MC commissioning was performed. The primary electron source was chosen to yield (for a 10 cm $\times$ 10 cm field at 0°), at a point laterally displaced 50 cm from the isocentre, the same fast neutron fluence as the one measured by the Bonner Sphere Spectrometer system (see section 2.4). The primary electron source was modelled as a Gaussian distribution centred at the chosen energy with a relative FWHM = 14% and a radial spatial distribution with FWHM = 1.5 mm. Additionally, different water depth–dose curves and profiles were generated from the MC phase space and compared with the measured data (depth profile mean deviation was below 2%).

The aim of theses simulations was to obtain the following:

- Neutron fluence spectra at the isocentre produced by the Siemens linac operating at different nominal energies (15, 18, 21, 25 MV) for different square fields.
- Neutron fluence spectra of the same machine operating at 15 MV at the location of the digital detector (see section 2.8) for nine different bunkers sizes (with the same height but different shapes and sizes covering the full range of typical treatment rooms, including bunkers 1 and 2 in Seville). In this case, each beam incidence was carried out in a single simulation, including the treatment room, the phantom and the linac.
- Neutron fluence spectra in all specific points in the phantom, for the head and neck (case (i)) and abdomen (case (ii)) treatments for linac installed in bunker 1. These spectra were calculated using an f5 tally (point detector). However, an additional simulation was performed using both f5 and f4 (flux averaged over cell) tallies to verify that the obtained results were equivalent.

All simulations were carried out using 48 double-processor computers, as a part of the cluster belonging to the Medical Physics Group, Department of Medical Physiology and Biophysics, University of Seville (Leal *et al* 2004).

2.4. Neutron spectrometry in the treatment room

Among the many available neutron spectrometry techniques, the multisphere or Bonner Sphere Spectrometer is the most used for radiation protection purposes (Thomas and Alevra 2002), owing to advantageous characteristics such as a wide energy range (from thermal to GeV neutrons), a large variety of active or passive thermal sensors that allow adapting the sensitivity to the specific workplace, a good photon discrimination and a simple signal management. The passive Bonner Sphere Spectrometer used in this work was described by Fernández *et al* (2007a, 2007b), including the response matrix analysis.

Following the standard terminology, $\Phi_E(E) \equiv (\mathrm{d}\Phi(E)/\mathrm{d}E)$ is the energy spectrum of the *absolute* neutron fluence so that the *total neutron fluence* is $\Phi = \int_E \Phi_E(E)\,\mathrm{d}E$. Similarly, $\varphi_E(E) \equiv (\mathrm{d}\varphi_E(E)/\mathrm{d}E)$ is the energy spectrum of the *unit* neutron fluence or *energy distribution of the neutron fluence* so that $\varphi = \int_E \varphi_E(E)\,\mathrm{d}E = 1$. It is, therefore, obvious that $\Phi_E(E) = \Phi\varphi_E(E)$ for any value of E. It is also common practice to represent neutron spectra in terms of lethargy, plotting the product $E \cdot \Phi_E(E)$ or $E \cdot \varphi_E(E)$ versus E (in the logarithmic scale). Such a plot has the visual property that equal areas below the graph represent equal neutron fluences.

In this work, the FRUIT code has been used for unfolding (Bedogni *et al* 2007), in order to obtain the energy distribution of the neutron fluence $\varphi_E(E)$ and the total neutron fluence Φ from the readings of the detectors at the centre of the Bonner spheres and from the evaluated response matrix. Ambient dose-equivalent values are subsequently evaluated from the $h^*(E)$ conversion coefficients (ICRU 1998) as

$$H^* = \int_E \Phi_E(E) \cdot h^*(E) \cdot \mathrm{d}E = \Phi \int_E \varphi_E(E) \cdot h^*(E) \cdot \mathrm{d}E. \tag{1}$$

Spectrometric measurements were made in all six irradiation facilities, with a static 10×10 cm^2 field at 0°, at a reference point located at the same height as the isocentre but laterally displaced 50 cm (without the NORMA phantom on the couch), as well as at the place where the digital detector is located (see section 2.8) (with NORMA) (Domingo *et al* 2009b, 2010a). This set of data allowed us to verify the MC simulation results for the Seville's facilities. Measurements were performed with statistical uncertainties of the order of 1%. The combination of these uncertainties with the response matrix uncertainties and with the ones related to the unfolding process allows us to determine fluence values with overall uncertainties in the range of 3–5% and ambient dose-equivalent values with uncertainties in the range of 4–7%.

2.5. PADC-based dosimeters

A miniaturized version of the Universitat Autònoma de Barcelona etched track neutron (PADC) dosimeters (García *et al* 2005, Domingo *et al* 2009b) has been used in this work to determine neutron fluence at all 16 specified points in the NORMA phantom (figure 1). Two extra dosimeters were placed on top of the digital detector for each irradiation condition. These 'miniature' dosimeters were obtained by cutting the standard (6×6) cm^2 dosimeter into nine equal (2×2) cm^2 pieces, which fit into our etching cells and which can be placed in the required spots (figure 1). The standard electrochemical etching procedure from Universitat Autònoma de Barcelona, described by Bouassoule *et al* (1999), has been applied. Track density

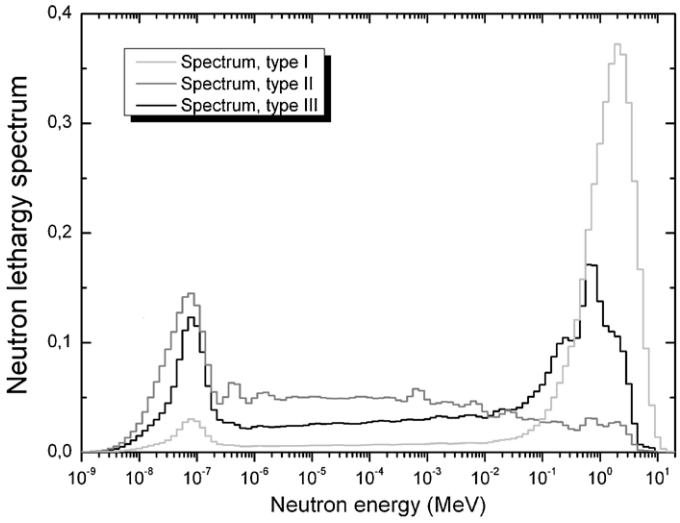

Figure 2. Neutron lethargy spectra of neutron fields supplied for calibration of the etched track neutron PADC dosimeters. Only spectra of types II and III were actually used for calibration purposes (see the text).

in the etched plates was measured using a semi-automatic counting system (Domingo *et al* 2009b).

The PADC dosimeters are sensitive to the whole energy range and their response had already been experimentally validated with ISO sources and realistic neutron fields as specified by the ISO standards (ISO 1998, 2000) at the Institut de Radioprotection et de Sûreté Nucléaire facilities (García *et al* 2005), as well as in quasi-monoenergetic neutron beams at the Institute for Reference Materials and Measurements from the European Joint Research Centre JRC-IRMM (Gëel, Belgium) Van der Graaf accelerator (Domingo *et al* 2009a).

PADC-based dosimeters are commonly calibrated for personal dosimetry in terms of personal dose equivalent H_p to characterize *external* irradiation of an individual. In this work, dosimeters are placed *inside* the NORMA anthropomorphic phantom and intend to measure the neutron field *inside* the phantom. Therefore, specific calibration irradiations of PADC dosimeters were carried out at the Physikalisch-Technische Bundesanstalt primary neutron facility to take into consideration the specific characteristics of neutron fields inside NORMA (previously estimated by the MC simulation, see the following text). Neutron irradiations took place free in air with the purpose of characterizing the dosimeter response in terms of fluence when placed in a location, no matter where, in the presence of a given neutron field. Three fluence energy distributions (see figure 2), and at different incidence angles to take into account the angular dependence, were used for calibration (Bedogni *et al* 2012, Domingo *et al* 2012). In table 3, the field spectral characteristics and calibration factors for the three different neutron calibration spectra are reported.

Fast neutrons appear from photoneutron–production reactions in the accelerator head and components. When they scatter in the room walls and other elements inside the treatment area, including the patient or the phantom, they become epithermal and thermal. Therefore, while the fast and the epithermal neutron components are highly directional, the thermal component can be approximated by an isotropic field at the point of measurement. This reasoning has

Table 3. Characteristics of the neutron fields used for calibration of the PADC-based dosimeters and the resulting fluence response.

	Spectrum type I	Spectrum type II	Spectrum type III
Description	^{252}Cf source	^{252}Cf(D2O+Cd) + Shadow block	^{252}Cf source + Shadow cone
Type	Fast	Epithermal+Thermal	Fast+Epithermal+Thermal
p_t	0.052	0.312	0.211
p_e	0.103	0.592	0.38
p_f	0.845	0.097	0.409
F_D (Tracks/neutron)	$(1.118 \pm 0.066) \times 10^{-4}$	$(4.65 \pm 0.48) \times 10^{-6}$	$(1.762 \pm 0.090) \times 10^{-5}$
F_{iso} (Tracks/neutron)	$(5.16 \pm 0.90) \times 10^{-5}$	$(2.15 \pm 0.24) \times 10^{-6}$	$(8.13 \pm 0.58) \times 10^{-6}$

p_t is the thermal fraction, p_e is the epithermal fraction, p_f is the fast fraction and F_D is the fluence response for normal incidence and F_{iso} for isotropic incidence.

been used to calculate the calibration factor F which converts tracks measured in the dosimeter (N^{PADC}) into fluence (Φ^{PADC}) in the following way:

$$\Phi^{PADC} = \frac{N^{PADC}}{F}, \qquad \text{where } F = (p_f + p_e) \cdot F_D + p_t \cdot F_{ISO} \tag{2}$$

with p_f, p_e and p_t being the fraction of fast, epithermal and thermal[19] neutrons in the spectrum considered, respectively, and F_D and F_{ISO} being the corresponding calibration factors for directional and isotropic incidences (see table 3).

Comparison of spectra in figure 2 with MC spectra at the phantom measurement points (figure 8) illustrates that calibration spectrum type II is the most representative for all measurement points, except for point 15, where spectrum type III is more adequate. Consequently, the particular calibration factor for a PADC dosimeter placed at point i in a given irradiation j is calculated as

$$\begin{aligned} &F^{i,j} = \left(p_f^{i,j} + p_e^{i,j}\right)F_D^{II} + p_t^{i,j}F_{ISO}^{II} \qquad \text{for } i \neq 15 \\ &\text{and} \\ &F^{i,j} = \left(p_f^{i,j} + p_e^{i,j}\right)F_D^{III} + p_t^{i,j}F_{ISO}^{III} \qquad \text{for } i = 15 \end{aligned} \tag{3}$$

where $p_f^{i,j}$, $p_e^{i,j}$ and $p_t^{i,j}$ are the corresponding fractions of fast, epithermal and thermal neutrons obtained from the MC simulation for the point and irradiation of interest, and F_D^{II}, F_{ISO}^{II}, F_D^{III} and F_{ISO}^{III} are the F_D and F_{ISO} calibration factors for spectra of types II and III, respectively (see table 3). The total neutron fluence at point i during irradiation j is subsequently evaluated from the reading $N_{i,j}^{PADC}$ of the corresponding dosimeter as

$$\Phi_{i,j}^{PADC} = \frac{N_{i,j}^{PADC}}{F^{i,j}}. \tag{4}$$

2.6. Li thermoluminiscence dosimeters

Standard ^{6}LiF/^{7}LiF pairs of dosimeters TLD-600/TLD-700 ($3 \times 3 \times 0.9$ mm^3 chips) have been used as an independent system to assess the thermal neutron fluences in the selected points inside NORMA.

TLD readouts have been carried out using a Harshaw reader, model 4000, with linear heating from room temperature up to 300 °C at a heating rate of 3 °C s^{-1}. A pre-irradiation

[19] We will use the conventional neutron classification according to their kinetic energy, i.e. thermal neutrons: up to 0.4 eV, the so-called Cadmium cut; epithermal neutrons: from 0.4 eV to 0.1 MeV; and fast neutrons: from 0.1 MeV to 20 MeV.

thermal treatment of 1 h at 400 °C, followed by a reproducible cooling down to room temperature, was always employed before reusing the detectors. Temperature and duration of the heating and cooling stages were properly controlled.

Neutron calibration was carried out at Physikalisch-Technische Bundesanstalt in scattered neutron reference radiation fields produced by a bare ^{252}Cf and a D_2O-moderated ^{252}Cf neutron source (Kluge *et al* 1997), and for gamma, using a ^{137}Cs calibration source at a secondary standard dosimetry laboratory in CIEMAT.

The methodology employed to analyse all the experimental glow curves obtained was based on the numerical techniques developed by Delgado and Gómez-Ros (1990, 1992) and Muñiz *et al* (1999, 2004). On the basis of the results of this glow curve analysis, thermal neutron fluences were obtained using the differences between TLD-600 and TLD-700 results for each measured point in NORMA (R) and the calibration factors as follows:

$$\Phi_{i,j}^{\mathrm{TLD}} = f_{600/700}^{n}\left[R_{600}^{i,j} - kR_{700}^{i,j}\right], \qquad k = \frac{f_{700}^{\gamma}}{f_{600}^{\gamma}}, \tag{5}$$

where the calibration factors used are $f_{600/700}^{n} = 488$ n cm^{-2} au (12%, $k = 2$) for neutrons and $f_{700}^{\gamma} = 1.86 \times 10^{-4}$ mGy au^{-1} (8%, $k = 2$) and $f_{600}^{\gamma} = 1.99 \times 10^{-4}$ mGy au^{-1} (10%, $k = 2$) for gammas.

2.7. Evaluation of neutron fluence, dose equivalent and equivalent dose

Both PADC and TLD passive detectors were used to evaluate the neutron fluence at each point i inside NORMA for each irradiation condition j, leading to the values $\Phi_{i,j}^{\mathrm{PADC}}$(4) and $\Phi_{i,j}^{\mathrm{TLD}}$(5), respectively. These measurements were repeated in all irradiation facilities listed in table 2. It is well known that ^{6}Li/^{7}Li TLD pairs allow a relatively precise estimation of the thermal neutron component, but they are insensitive to the epithermal and fast components. On the other hand, the PADC response is well characterized for fast neutrons, but relevant to large uncertainties appearing in the epithermal and thermal ranges. Taking all that into account, the best estimation of fluence is calculated by combining the measurements of both detectors as follows:

$$\Phi_{i,j} = \Phi_{i,j}^{\mathrm{TLD}} + \left(p_{\mathrm{e}}^{i,j} + p_{\mathrm{f}}^{i,j}\right)\Phi_{i,j}^{\mathrm{PADC}}. \tag{6}$$

Uncertainties for the best estimation of the total fluence are obtained from standard propagation of uncertainties of the TLD and PADC measurements and are expressed at the standard (1SD) level.

Absorbed dose is the most useful measurable quantity, as it allows protection quantities to be evaluated from tabulated weighting factors. Unfortunately, it is extremely difficult in practice to measure the absorbed dose due to neutron irradiation because of the complexity of neutrons interaction mechanisms with matter. All secondary charged particles originating around the volume of interest would have to be considered and their energy deposition inside the region of interest would have to be evaluated.

Alternatively, in the kerma approximation, the absorbed dose can be approximated by kerma which, in turn, may be evaluated from fluence through the kerma factors. In this situation, neutron dose-equivalent value H in a tissue-like point might be obtained from the appropriate kerma factors $k(E)$ and the radiation quality factors $Q(E)$ as

$$H_{i,j} = \Phi_{i,j}\int_{\mathrm{E}} k(E)\cdot Q(E)\cdot \varphi_{i,j}(E)\cdot \mathrm{d}E, \tag{7}$$

where the measurable quantities, i.e. the total neutron fluence $\Phi_{i,j}$ and its energy distribution $\varphi_{i,j}$, have been determined in this work for all points of interest for different irradiation

conditions. In practice, $Q(E)$ is not easy to evaluate, as Q depends on the linear energy transfer L of the incoming particle in the absorber, which in turn is a function of its energy E. On the other hand, the current ICRP (2007) recommends evaluating equivalent doses in a tissue H_T from the absorbed dose in this tissue D_T and the radiation weighting factors $w_R(E)$ (see ICRP publication 92 (ICRP 2003) for extensive discussion about the usage of w_R and Q, in particular for neutron irradiation). Equivalent doses in a tissue are good estimators of dose equivalent in the kerma approximation, except for low-energy neutrons (below 1 MeV), because the energy deposited by the secondary photons originated locally by H(n,γ)D reactions is included in Q, but excluded in the w_R for neutrons. Nevertheless, the values of $k(E)$ and $w_R(E)$ (or $Q(E)$) for low-energy neutrons make small contribution to dose.

Hence, we evaluate the equivalent dose in a tissue or organ for a measurement point i and irradiation j as

$$H_T^{i,j} = \Phi_{i,j} \int_E k(E) \cdot \varphi_{i,j}(E) \cdot w_R(E) \cdot dE, \tag{8}$$

where $\Phi_{i,j}$ is evaluated from (6), $\varphi_{i,j}(E)$ is the neutron fluence distribution obtained by the MC simulation, $w_R(E)$ the neutron radiation weighting factor and $k(E)$ is the kerma factor of the absorber inferred by Siebert and Schuhmacher (1995) for ICRU tissue.

Therefore, a complete set of equivalent doses in multiple organs could be generated for the two types of treatments in all facilities.

2.8. The digital detector

A thorough description of the detector was given by Gómez *et al* (2010) and Domingo *et al* (2010b). This system is composed by an array of static random access memories (SRAM) devices which are sensitive to neutron fluence (Baumann and Smith 2001). Single-event upsets of memory states are produced in the detector because of the interaction with thermal neutrons. The number of these upsets (or events) is proportional to the neutron fluence arriving to the detector placed inside the treatment room.

The detector design represents in practice not a single detector but a plurality of detectors (taking into account that each memory cell is a threshold detector by itself), which overcomes the problem of signal pile-up probability ($\sim 10^{-9}$). No saturation effects have been observed, since the large size of memory cells available in the detection system (5.4×10^8), the fraction of SRAM cells occupied by upsets in these measurements, are always below 3×10^{-5}.

The system operates as follows: before each irradiation, the memory content is set to a fixed pattern and, after exposure to radiation, the memory content is read and the amount of upsets is computed. A piece of software has been written in LabVIEW© (2009 National Instruments) to control all these processes and also to finally convert events into neutron-equivalent doses. The software is available from the authors on request.

The digital detector was located during all irradiations in front of the rotation gantry axis and close to the wall to avoid interference with the patient or with the staff (see the inset of figure 1). Preliminary experiments concluded on the feasibility of such location given that both the fluence and the detector response are almost constant under the same irradiation conditions irrespective of gantry angle (Jiménez-Ortega *et al* 2011). Robustness and reliability of the neutron detector system have been verified since it has been used for more than four years in different clinical linac facilities.

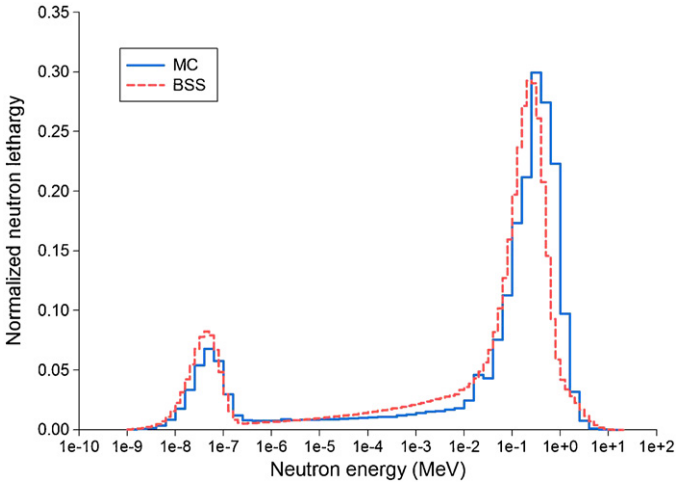

Figure 3. Normalized neutron lethargy spectra at 50 cm from the isocentre for the Siemens PRIMUS operating at 15 MV in bunker 1 obtained by the MC simulation (MC) and measurements with the Bonner Sphere Spectrometer (BSS).

3. Results and discussion

For exposures in NORMA, the neutron-equivalent dose in a given organ k for a specific treatment j, $H^{k,j}_{\mathrm{T,NORMA}}$ can be evaluated from the $H^{i,j}_{\mathrm{T,NORMA}}$ values obtained for the points i closest to the specific organ k (table 1). In order to make such calculations, and according to (8), neutron spectra and total fluence for each (i, j) situation were required.

3.1. Neutron spectra

The aim of the MC simulation, together with the neutron spectrometry, was to provide a normalized neutron spectrum for each calculation point and treatment type. The full MC simulation generated a complete model of neutron spectra for the Siemens machine at any point inside the bunker or the phantom for the head and abdomen treatments. Then, a study on the dependence of these spectra on nominal energy, machine manufacturer, field size, gantry angle and treatment location was carried out.

3.1.1. MC and experimental spectrum agreement. The MC simulations of neutron energy fluence reproduce the measured spectra with the Bonner Sphere Spectrometer at 50 cm from the isocentre and at the digital detector position. Figure 3 depicts the results per unit fluence. As the Bonner Sphere Spectrometer is a standard system for neutron spectrometry, the agreement found confirms that our MC calculations, which represent a key ground of the model, correctly simulate the neutron transport process.

3.1.2. Energy dependence. The MC simulation revealed that when varying nominal energy from 15 to 25 MV at the isocentre, for a specific linac and bunker geometry, the total neutron fluence increases (see figure 4(a)). Nevertheless, as displayed in figure 4(b), the normalized spectra exhibit very small dependence on accelerator energy. Differences observed in figure 4(a) are only due to the photonuclear cross section dependence on energy, which

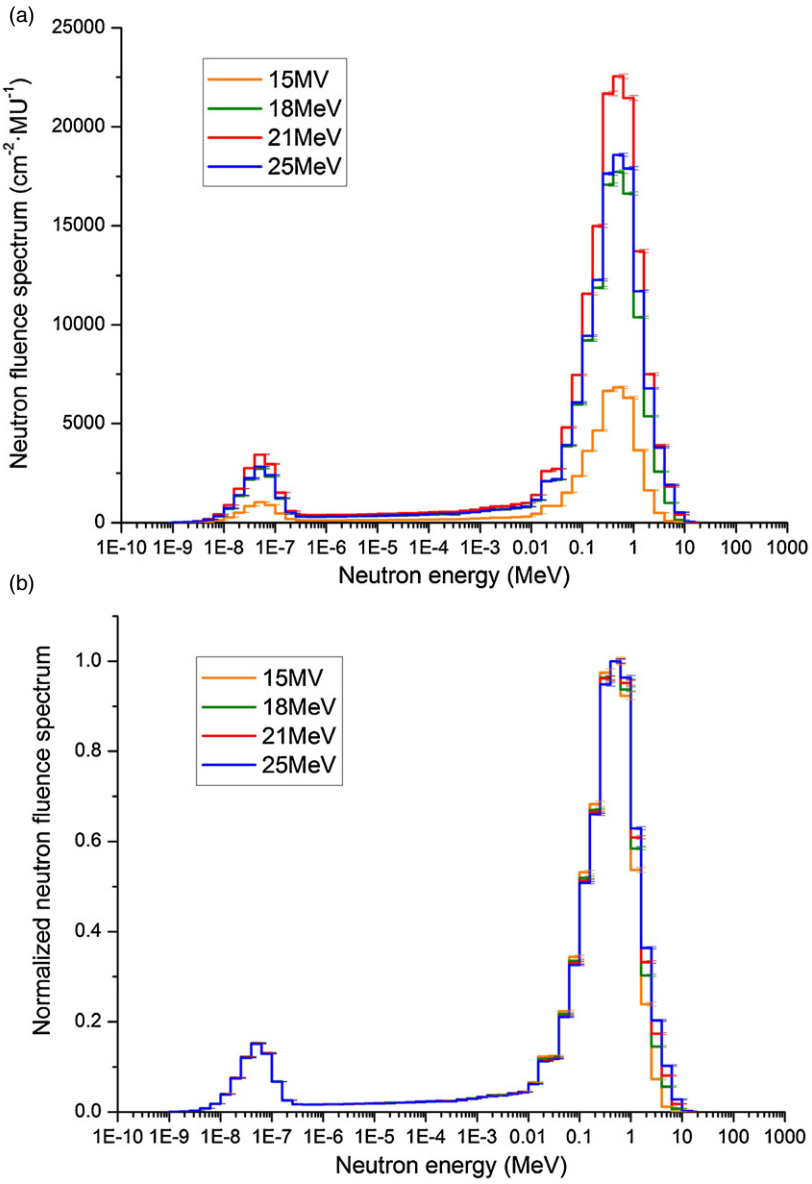

Figure 4. (a) The MC simulation of neutron fluence spectra per monitor unit (cm^{-2} MU^{-1}) at the isocentre for a Siemens PRIMUS machine operating at different nominal energies from 15 to 25 MV as if installed in bunker 1. (b) Normalized neutron fluence spectra under the same conditions. Error bars represent the statistical uncertainty of simulations.

affects the total number of neutrons generated. In fact, the neutron-production mechanism is mainly evaporation, with a single peak around 1 MeV.

This behaviour was confirmed by experimental measurements with the Bonner Sphere Spectrometer at 50 cm from the isocentre (without phantom on the couch) (see figure 5(a)). Indeed, the height of fast peak increases with the nominal energy (15, 18 and 23 MV).

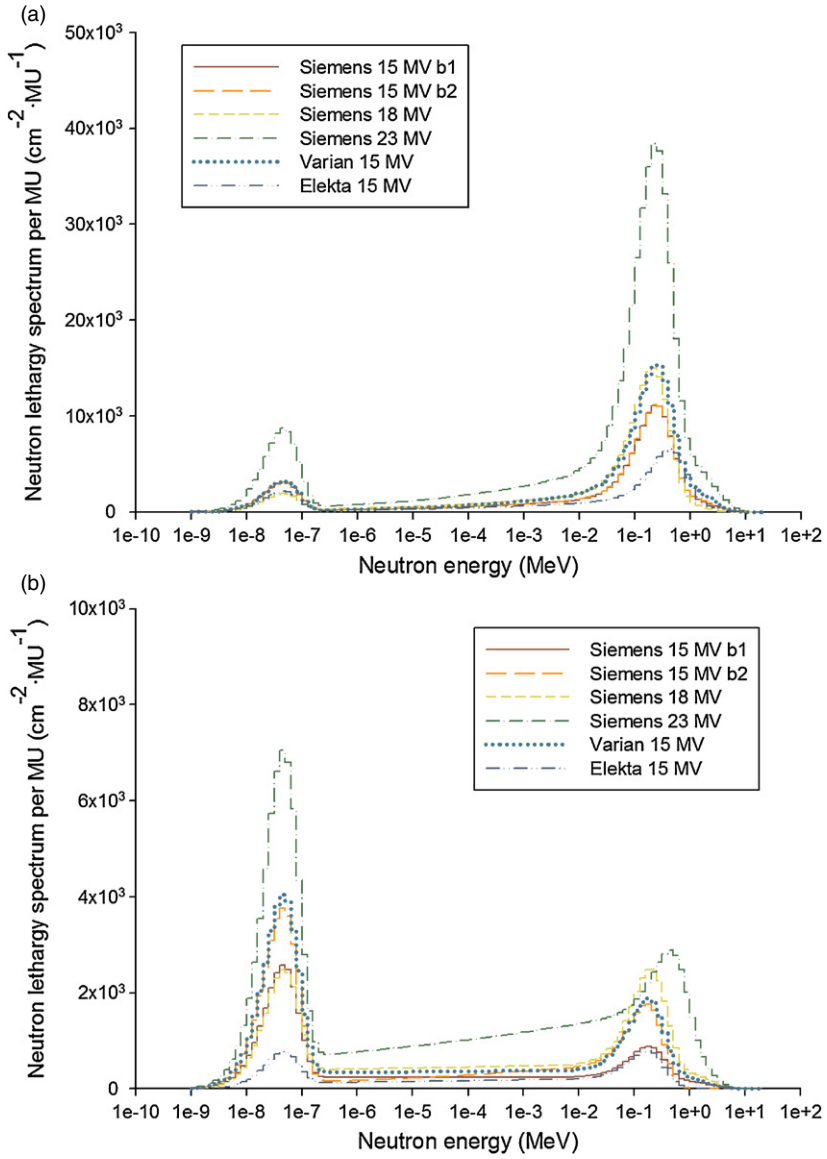

Figure 5. Neutron lethargy spectra per MU measured with the Bonner Sphere Spectrometer (BSS) (a) at 50 cm from the isocentre (without phantom) and (b) at the digital detector position (with the phantom). Note that the distance from the BSS to the source is different for each installation in plot (b), as the digital detector is placed close to the wall and thus detector position depends on the bunker size.

3.1.3. Manufacturer dependence. Neutron spectra for the Elekta, Varian and Siemens machines involved in this study were measured with the Bonner Sphere Spectrometer at 50 cm from the isocentre (without phantom on the couch) (figure 5(a)). The shapes of the neutron spectra (per MU) are the same as the ones obtained with MC at the isocentre (figure 4(a)), with a predominant fast component. However, for the same nominal energy, neutron fluence varies

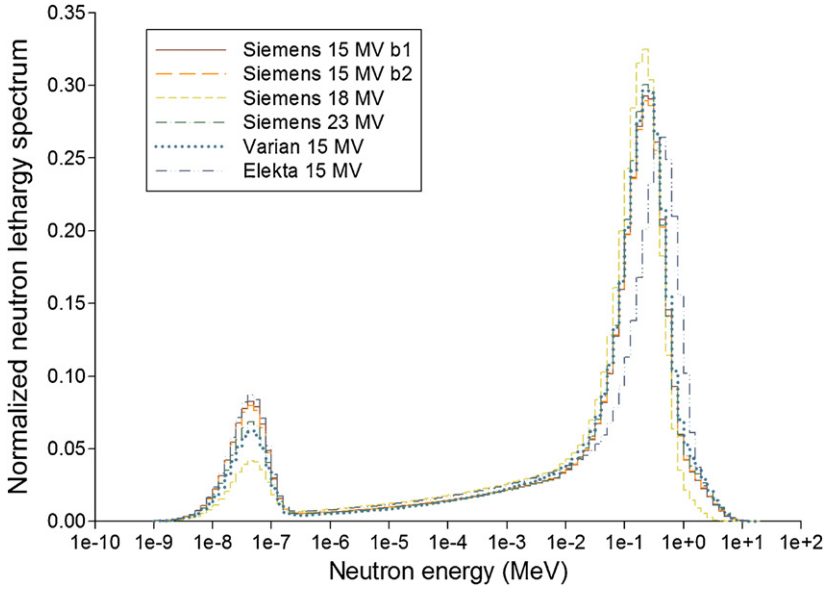

Figure 6. Normalized neutron lethargy spectra at 50 cm from the isocentre measured with the Bonner Sphere Spectrometer.

with linac manufacturer, with Varian and Elekta being the machines leading to the highest and lowest values, respectively. This difference among manufacturers makes that neutron production in a 15 MV Varian machine is approximately the same as in a 18 MV Siemens machine. The larger epithermal tail for the 23 MV spectra, together with a displacement of the fast neutron peak to higher energies, could be explained by the direct neutron-production process, which becomes significant at higher energies.

The same set of measurements was repeated at the digital detector position and with the phantom on the treatment couch (figure 5(b)). The relative sizes of thermal and fast regions have now changed with respect to figure 5(a) as a consequence of the larger distance to the source. The fast peak decreases owing to the inverse square law and to the fast neutrons absorption inside the patient. This fast neutrons moderation increases the epithermal component. Thermal fluence is almost unaffected by the distance as they behave like a 'neutron cloud' (Pena *et al* 2005). It is observed that the thermal component depends on the primary neutrons spectra generated inside the linac head (i.e. the highest and lowest fast peaks in figure 5(a) coincide with the highest and lowest peaks in 5(b), respectively).

The normalized spectra (neutron lethargy spectra per unit fluence), measured at 50 cm from the isocentre (figure 6), revealed that all spectra are the same (with uncertainties that are around 3% at the peaks and up to 10% outside the peaks, at worst). The apparent differences displayed in figure 5(b) stem from the fact that the machines are installed in different sized bunkers (see table 2 and section 3.1.7).

The above confirms the prominence of a common evaporation process during neutron production and that the main differences between manufacturers lie only in the total number of neutrons generated. However, the direct neutron–production process seems to become more important at higher energies, and it could be the reason for the small deviation observed for the 23 MV spectra.

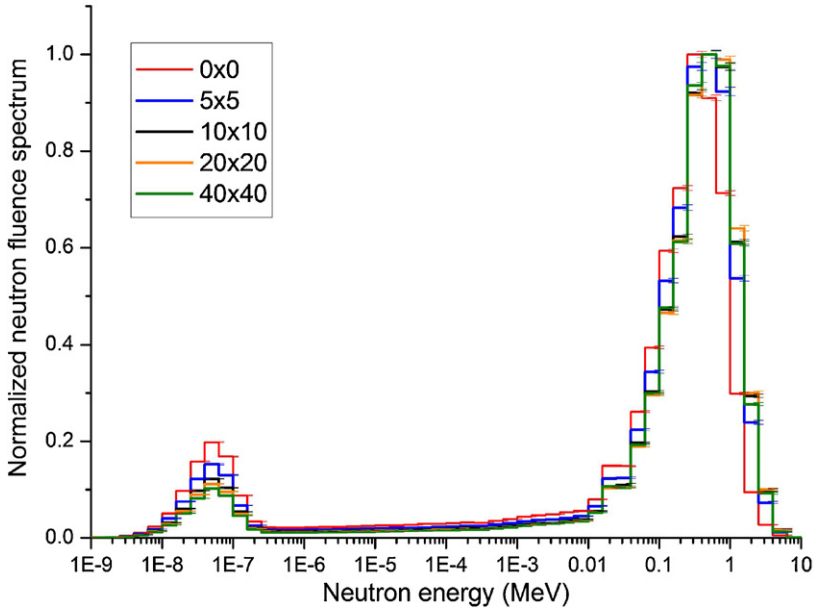

Figure 7. Normalized neutron fluence spectra obtained by the MC simulation of a Siemens PRIMUS machine operating at 15 MV in bunker 1 for field sizes ranging from 0 × 0 to 40 × 40 cm^2, at the isocentre. Error bars represent the statistical uncertainty of simulations.

Therefore, in the energy range mostly used for photon beam radiotherapy (energies in excess of 18 MV are rarely used), it is a very good approximation to considerer that, regardless of the machine manufacturer and energy, the patient will be exposed to the same energy distribution of neutrons.

3.1.4. Field size dependence. Figure 7 depicts the normalized neutron fluence spectra obtained by MC simulations with different field sizes. The spectra are independent of the field size. This result was confirmed by the total neutron fluence measured with passive detectors inside NORMA for field sizes ranging from 2 × 2 to 20 × 20 cm^2 (irradiation setups (iii) and (vi)), at the different institutions involved in this study.

The above explains the fact that, in the measurements carried out at Seville's bunker 1, the digital detector readings under the irradiation conditions (i) and (ii), and under intensity-modulated (IMRT) head and abdomen treatments, matched (within the uncertainties). Effectively, while the intensity modulation of treatment fields is generally reached through the contribution of a variety of field sizes (segments), from the point of view of neutron contribution, the open and intensity-modulated beams are equivalent (provided the beam-on time is the same).

This result allowed us to reproduce the complex real IMRT plans as simpler plans with the same MU per beam incidence but with open beams instead, making the multi-institution measurements easier. Furthermore, it implies a very important simplification regarding neutron dosimetry.

3.1.5. Gantry angle. MC simulations showed that neutron fluence spectra inside NORMA at different gantry angles are the same for midline points. For other points, the heights of the thermal and fast peaks change depending on the point depth at each angle.

Table 4. Weight of each neutron component of the simulated fields in the NORMA points.

	Head treatment			Abdomen treatment		
	p_t	p_e	p_f	p_t	p_e	p_f
1	0.739	0.183	0.078	0.748	0.187	0.064
2	0.875	0.085	0.041	0.903	0.071	0.026
3	0.814	0.133	0.053	0.823	0.129	0.048
4	0.807	0.140	0.053	0.837	0.122	0.041
5	0.823	0.132	0.045	0.823	0.133	0.044
6	0.821	0.133	0.045	0.824	0.131	0.045
7	0.597	0.261	0.142	0.584	0.263	0.152
8	0.597	0.261	0.142	0.581	0.266	0.154
9	0.719	0.196	0.085	0.697	0.208	0.095
10	0.738	0.187	0.075	0.697	0.201	0.101
11	0.923	0.054	0.023	0.903	0.065	0.032
12	0.855	0.111	0.034	0.817	0.134	0.049
13	0.905	0.075	0.020	0.875	0.094	0.031
14	0.902	0.078	0.019	0.874	0.093	0.032
15	0.330	0.267	0.403	0.276	0.275	0.449
16	0.863	0.101	0.036	0.648	0.186	0.166

p_t is the thermal fraction, p_e is the epithermal fraction and p_f is the fast fraction.

The same result was found in experimental measurements under setups (vi) and (vii). Irradiations at 0° and 270° did not lead to significant changes in the in-phantom fluence measured with PADCs and TLDs at midline points (2 and 11). However, when symmetrical positions were tested, such as 7/8 and 13/14, relative differences of up to 50% were measured (particularly in the lung).

Nevertheless, in real treatments, beam entry angles usually follow a circular geometry around the isocentre which cancels out this angle dependence. Single boost beams can sometimes be used, but this strategy usually involves low-energy beams which have low neutron contribution.

3.1.6. Treatment location. In order to analyse how the treatment location affects the neutron field inside the patient, full MC simulations of the irradiation conditions (i) and (ii) for the 15 MV Siemens linac were carried out for all 16 points inside NORMA (figure 8).

Fast neutrons are moderated through interactions inside the phantom. Therefore, superficial localizations, such as skin, reveal a predominant fast component that decreases in the case of deeper positions. In general, neutron contamination in a given point depends on the distance from this point to the treatment isocentre. For instance, at the thyroid (4), thermal neutron fluence is higher during a head treatment than during an abdomen treatment, whereas at the pelvic point (12), the opposite happens. Table 4 shows the fast, epithermal and thermal fractions of the simulated neutron spectra for all points in NORMA, for the head and abdomen treatments.

Considering all previous results, we conclude that it is appropriate to use a unique normalized neutron spectrum for each calculation point and treatment location (head or abdomen) inside the patient ($\varphi_{i,j}(E)$), regardless of the nominal energy, machine manufacturer, field size and entry angle. This result implies a very important generalization for our methodology which simplifies and enhances the applicability of the model.

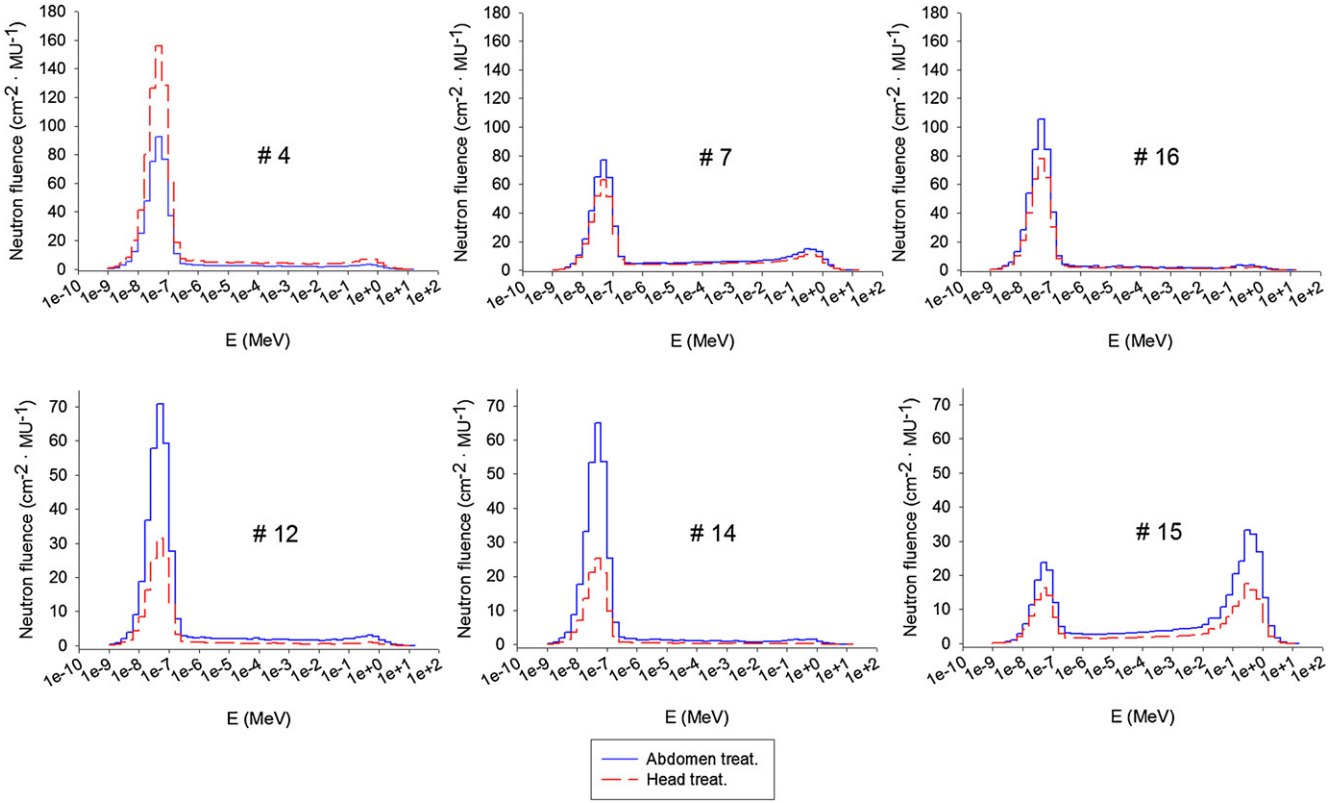

Figure 8. Neutron fluence spectra simulated inside NORMA for a Siemens linac of 15 MV in head and neck, and abdomen treatments (irradiations (i) and (ii)). Six points have been chosen for displaying the results. All points are peripheral for both treatments so that comparison makes sense.

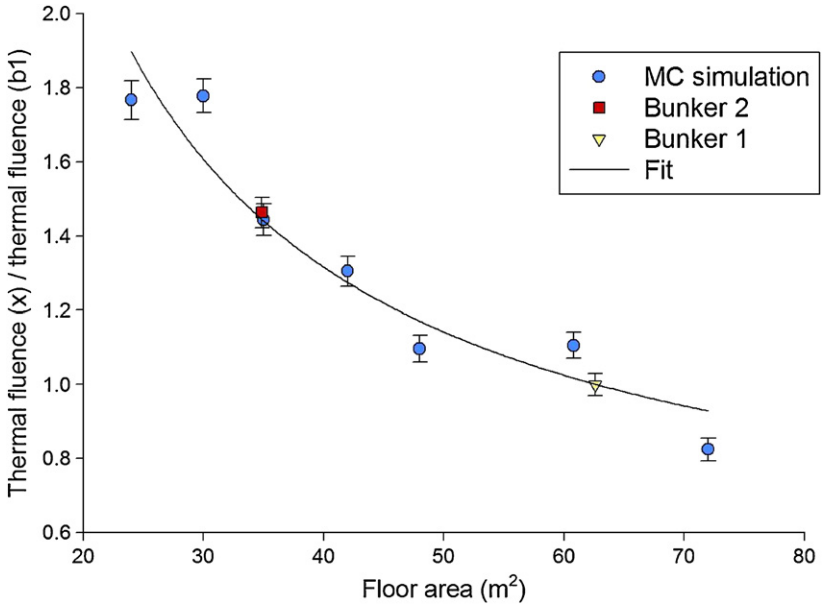

Figure 9. Ratios between thermal neutron fluence for bunkers of different floor areas and the fluence at bunker b1 obtained by the MC simulation (black dots). The solid line represents the fitting function F_A (area floor factor) to the simulated data. The floor area does not include the maze. Grey points represent the values of the bunker 1 and 2 geometries. Error bars represent the statistical uncertainty of simulations.

3.1.7. Bunker size dependence. As stated above, thermal neutron fluence inside the bunker is rather independent of position (without the patient) but dependent on room volume: the larger the room, the lower the thermal neutron fluence (i.e. volumetric neutron density) (Pena *et al* 2005). Measurements carried out with the Bonner Sphere Spectrometer agree with this.

Effectively, in figure 5(a), both Seville's bunkers spectra matched perfectly but they split in figure 5(b). The reason for that lies in the fact that the larger the room, the larger the distance from the source to the measurement point, and the fast neutron fluence decreases (smaller for bunker 1 in Seville). Besides, given that thermal neutron fluence decreases with the bunker size, thermal fluence of bunker 1 is also smaller.

In order to model this dependence, nine MC simulations for different floor room areas (without the maze) were carried out. Figure 9 depicts the ratios between the thermal neutron fluence in each room and the fluence at bunker 1 in Seville. These data were successfully fitted ($R^2 = 0.92$) by the following function:

$$F_A = a + \frac{b}{A}, \tag{9}$$

where A represents the floor area (m^2) and $a = 0.396 \pm 0.027$ and $b = 37.3 \pm 1.1$ (m^2) are the fitting parameters. The F_A function will be later feed into the model.

The MC estimations were independently checked by means of the digital detector (only sensitive to thermal neutrons). Effectively, F_A for bunker 2 in Seville (same linac) is 1.46 ± 0.04, whereas the experimental value was 1.43 ± 0.03. Moreover, the same ratio obtained from thermal peaks in figure 5(b) also resulted in 1.46.

3.2. Total fluence

In order to complete the benchmark dataset, the total fluence measurements with passive detectors inside NORMA for the (i) and (ii) irradiation conditions were carried out so that $\Phi_{i,j}$ values were obtained according to (6), using the corresponding fast, epithermal and thermal fractions (table 4). Results are plotted in figure 10 with their uncertainties (1SD), together with the MC total fluence estimation for the irradiation at Seville bunker 1. For both treatments, in most of the points at which measurements from both TLDs and PADCs were available, MC and experimental data agreed within 1SD of the experimental data. Larger deviations were found only for a few points, but all of them within 2SD. These results confirm that the methodology suggested in (6) to determine the total fluence with passive detectors is sound for both spectral types (i.e. spectra with almost no fast component and spectra where thermal and fast components are comparable, as is the case for lungs or skin).

3.3. Neutron-equivalent dose in peripheral organs

Neutron-equivalent doses for each point inside NORMA were subsequently evaluated using (8), on the basis of the total fluence values estimated from the passive detectors measurements. Figure 11 depicts equivalent dose results for the head treatment. Plot 11(a) displays the values for treatments at different nominal energies, showing that for higher MV modalities, the neutron dose-equivalent values are higher, especially in points close to the treatment area. The biggest differences among neutron-equivalent doses appear at skin and lungs, where a relevant fast neutron component, from the primary neutrons originated in the accelerator head, is still present. At the remaining points, located deeper in NORMA, neutrons have propagated inside the phantom and they have been strongly moderated. Plot 11(b) shows the differences in neutron-equivalent doses when linacs from different manufacturers are considered. As expected, the Varian linac is the machine leading to the highest values. Results for the abdomen treatment are not displayed, but present the same trends.

These results evidence that for a fixed treatment location it is a reasonable approximation to consider that a change in the energy or the linac manufacturer has the only effect of raising, or lowering, the neutron-equivalent doses by a unique scaling factor, regardless of the particular point considered inside NORMA. This scaling factor could be determined by the readings of the digital detector. However, given that this detector is mainly sensitive to the thermal neutron component, different readings are obtained for bunkers of different sizes in spite of the fact that the same treatment is delivered by the same linac. This is the case of the results in the two bunkers with the Siemens PRIMUS 15 MV. The digital detector readings are different, while neutron-equivalent dose values evaluated in all 16 points in NORMA agreed within the uncertainties. Thus, a correction factor $1/F_{\mathrm{A}}$ (9) must be applied to correct the effect of bunker size on the digital detector readings.

Figure 12 displays the averaged ratio, from all the installations, of the equivalent dose values at the 16 measurement points in the phantom to the corrected digital detector readings for both the analysed treatment locations. Despite differences among irradiation conditions, and as was expected, results at each point for each type of treatment have shown relatively small dispersions (30%, 1SD), it is possible to assign an average value (in equivalent dose units) to each point. As a result, at each point and for each treatment, a set of factors ($f^n_{i,j}$) expressed in units of neutron-equivalent dose could be obtained, in order to convert the digital detector reading into in-phantom (or in-patient) neutron-equivalent dose with an uncertainty of 30%, which is acceptable for personal dosimetry as indicated in the current recommendations for monitoring individuals (European Commission 2009).

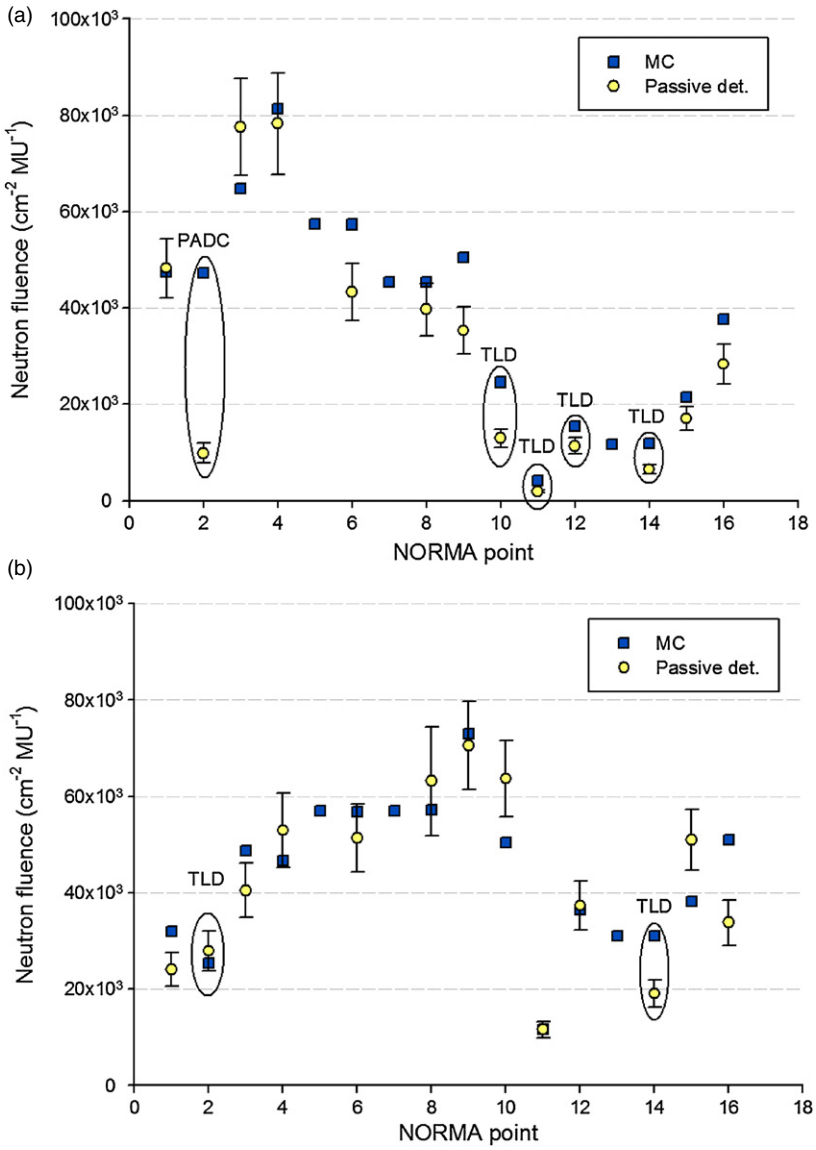

Figure 10. Total fluence as measured by passive detectors at each point in NORMA for both treatment types ((a) head and neck and (b) abdomen) carried out in Seville's bunker 1, for which the MC simulation (MC) is available. Only one of the symmetrical pair points (i.e. 6, 8 and 14) was measured. PADC measurements at points with a very low fast neutron fluence ($\sim 10^4$ cm^{-2} UM^{-1} approximately) could not be used and the total neutron fluence was reported only by TLD readings (thermal fluence) (marked in the plot with 'TLD'). Point 2 in plot (a) (isocentre, thus not relevant for peripheral dose) was reported only by PADCs as TLDs did not respond properly because of the high photon fluence. PADC fluence measurements uncertainty ranges between 11% and 58% (being the latter for specific points where fast fluence was very low and thus close to their detection limit). Most of the PADC uncertainty values are of the order of 15%. Uncertainty associated with fluence estimation by TLDs is also around 15% (1SD).

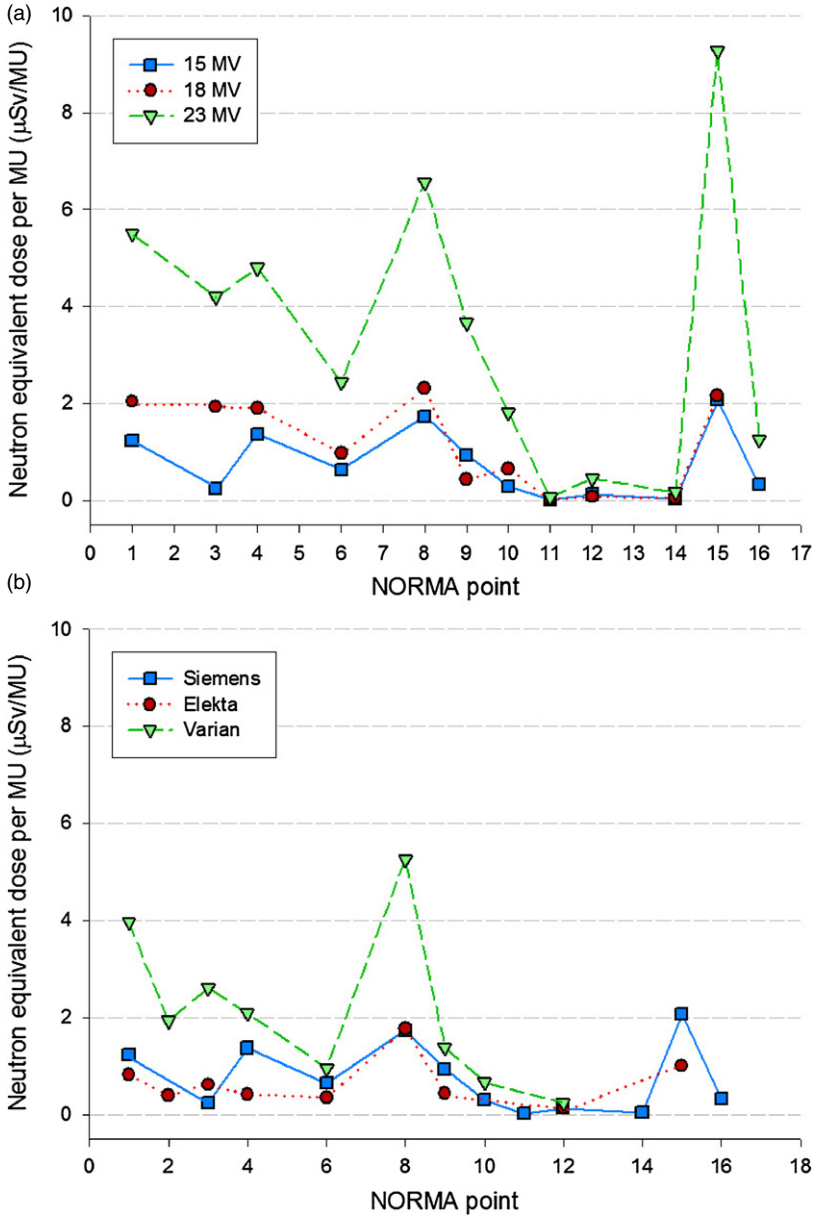

Figure 11. Equivalent dose estimations in the selected 16 locations in NORMA phantom for the head treatment (irradiation (i)) in (a) a Siemens linac (at 15, 18 and 23 MV) and (b) for different linac manufacturers (Siemens, Varian, Elekta) all of them at 15 MV.

Thus, the neutron-equivalent dose in an organ for point i of a patient undergoing a treatment j ($H^{i,j}_{\mathrm{T,patient}}$) may be obtained from the digital detector reading (number of events) during the patient exposure $DD^{j}_{\mathrm{patient}}$ from the following model:

$$H^{i,j}_{\mathrm{T,patient}}(\mu Sv) = \frac{DD^{j}_{\mathrm{patient}}}{F_{\mathrm{A}}} \cdot f^{n}_{i,j}, \tag{10}$$

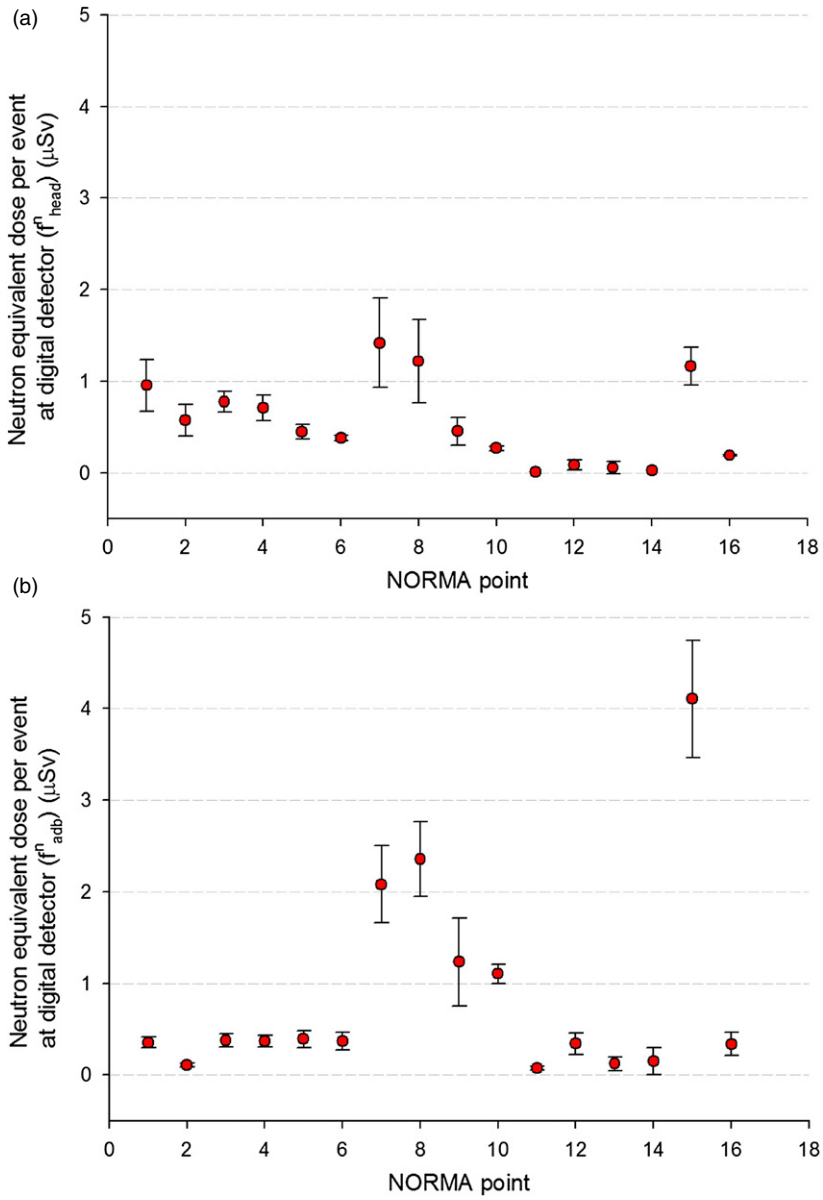

Figure 12. Averaged ratio of the equivalent doses per event at the digital detector, evaluated in all 16 measurement points in the phantom. The digital detector readings were normalized to Seville's bunker 1 by means of the $1/F_A$ factor. Averaged values were calculated for all the installations described in table 2. (a), b) The results for the head (irradiation (i)) and the abdomen (irradiation (ii)) treatments.

where $f^n_{i,j}$ are the appropriate factors obtained from exposures in NORMA, $f^n_{i,j}(\mu Sv/\text{event}) = \frac{H^{i,j}_{T,NORMA}}{DD^j_{NORMA}}$ (figure 12) and F_A takes into consideration the actual bunker size where treatment takes place.

Finally, for patient neutron-equivalent doses in a given organ k for the specific treatment j, $H^{k,j}_{\mathrm{T,patient}}$ are evaluated from the $H^{i,j}_{\mathrm{T,patient}}$ values obtained for the points i closest to the specific organ k (table 1).

We have showed that the use of these factors for irradiations in several installations led to deviations of 30% in the assignment of values of peripheral neutron-equivalent doses in an organ. Nevertheless, it could be possible to obtain a higher precision if dedicated measurements with both the digital detector and NORMA were performed in the particular installation of interest, in order to obtain specific factors for that installation.

4. Conclusions

A complete methodology and a benchmark data set have been developed to carry out a real-time assessment of the distribution of neutron-equivalent doses in organs for patients undergoing photon radiotherapy treatments. Those values are estimated with an overall uncertainty of the order of 30%, which is an acceptable level given the complexity of the neutron dosimetry problem. The main sources of uncertainties are the total neutron fluence measured with passive detectors, and the use of a unique set of calibration factors regardless of the irradiation facility. In summary, for a given treatment location (either head or abdomen), it is possible to obtain the value of the equivalent neutron dose in any organ of the patient from the properly digital detector readings (corrected by room size), regardless of the installation and the particular conditions of the accelerator used. This model has been built into a piece of software, associated with our digital detector, in order to provide real-time neutron-equivalent dose distribution in specific organs in the patient. However, the same methodology would be applicable to other neutron-sensitive detectors, following a specific calibration procedure.

It is worth noting one of the most important intermediate results leading to the proposed model: the primary normalized neutron spectra exhibit an almost equal distribution at the isocentre for the considered linacs and energies. This universality of the primary spectral distributions can be extended so that the moderated in-phantom neutron spectra are also equal for the different installations. Consequently, a unique normalized neutron spectra specific for each calculation point and treatment type can be used.

This effort should facilitate important consequences in modern radiotherapy, as it will be possible to make an estimation of equivalent neutron-dose distributions for each patient under his/her particular irradiation conditions. This piece of information is essential in order to perform future correlations with clinical data regarding secondary cancers which might help to improve current risk-estimation models.

Acknowledgments

The authors are indebted to the Andalusian Health Service (SAS) for its support through a University Law (LOU) contract with the University of Seville, to the Spanish Ministry of Industry, Tourism and Trade (through PROFIT programme), to the Innovation Agency of the Andalusian Government, to the Andalusian Technology Corporation and to the Caja San Fernando Foundation for their financial support. The authors would also like to thank the Spanish Ministry of Science and Technology for its support through grant agreements PET2006-0412, FIS2006-01843, FIS2009-10634, to the Catalan Research Management Agency (AGAUR) for its support through grant 2009SGR-122 and, especially, to the Spanish Nuclear Safety Council (CSN) for its support through a specific agreement with the University of Seville for measuring neutron doses in radiotherapy patients. The authors would like to

express their gratitude to Mariano García-Alvez and Alejandro Revuelta for their support in phantoms manufacturing.

References

Baumann R and Smith E 2001 Neutron-induced B-10 fission as a major source of soft errors in high density SRAMs *Microelectron. Reliab.* **41** 211–8

Bednarz B, Hancox C and Xu X G 2009 Calculated organ doses from selected prostate treatment plans using Monte Carlo simulations and an anatomically realistic computational phantom *Phys. Med. Biol.* **54** 5271–86

Bedogni R, Domingo C, Esposito A and Fernández F 2007 FRUIT: an operational tool for multisphere neutron spectrometry in workplaces *Nucl. Instrum. Methods Phys. Res.* A **580** 1301–9

Bedogni R, Domingo C, Esposito A, Gentile A, Garcia-Fusté M J, de-San-Pedro M, Tana L, d'Errico F and Di Fulvio A 2012 Calibration of PADC-based neutron area dosemeters in the neutron field produced in the treatment room of a medical LINAC *Radiat. Meas.* (at press) doi:10.1016/j.radmeas.2012.04.009

Bouassoule T, Fernández F, Marin M and Tomas M 1999 A dosemeter based on nuclear track etched detectors for thermal, fast and high energy neutrons with flat response *Radiat. Prot. Dosim.* **85** 39–43

Delgado A and Gómez-Ros J M 1990 A simple method for glow curve analysis improving TLD-100 performance in the dose region below 100 mGy *Radiat. Prot. Dosim.* **34** 357–60

Delgado A and Gómez-Ros J M 1992 Glow curve analysis: a method for improving TLD reliability *Radiat. Prot. Dosim.* **43** 143–6

Domingo C, de-San-Pedro M, García-Fusté M J, Romero M T, Amgarou K and Fernández F 2012 Estimation of the response function of a PADC based neutron dosimeter in terms of fluence and $H_p(10)$ *Radiat. Meas.* (at press) doi:10.1016/j.radmeas.2012.02.016

Domingo C, García-Fusté M J, Amgarou K, Morales E and Castelo J 2009a Measurements in quasi-monoenergetic neutron beams at the EC-IRMM Van-der-Graaf accelerator for calibration of the UAB PADC based neutron dosimeter *Radiat. Meas.* **44** 981–4

Domingo C, García-Fusté M J, Morales E, Amgarou K, Castelo J and Sánchez-Doblado F 2009b Evaluation of neutron doses received at different organs in radiotherapy treatments using the UAB PADC based dosemeters in an anthropomorphic phantom *Radiat. Meas.* **44** 1073–6

Domingo C *et al* 2010a Neutron spectrometry and determination of neutron ambient dose equivalents in different linac treatment rooms during radiotherapy *Radiat. Meas.* **45** 1391–7

Domingo C *et al* 2010b Calibration of a neutron detector based on single event upset of SRAM memories *Radiat. Meas.* **45** 1513–7

European Commission 2009 Technical recommendations for monitoring individuals occupationally exposed to external radiation *Radiation Protection Publication 160*

Fernández F, Bouassoule T, Amgarou K, Domingo C, García M J, Lacoste V, Gressier V and Muller H 2007b Monte Carlo calculations and validation of a gold foil-based Bonner sphere system *Radiat. Prot. Dosim.* **126** 366–70

Fernández F, Domingo C, Amgarou K, Castelo J, Bouassoule T, García M J and Luguera E 2007a Neutron measurements in a Varian 21006 linac facility using a Bonner system based on passive gold activation detectors *Radiat. Prot. Dosim.* **126** 361–5

García M J, Amgarou K, Domingo C and Fernández F 2005 Neutron response study of two CR-39 personal dosemeters with air and Nylon converters *Radiat. Meas.* **40** 607–11

Gómez F, Iglesias A and Sánchez-Doblado F 2010 A new active method for the measurement of slow-neutron fluence in modern radiotherapy treatment rooms *Phys. Med. Biol.* **55** 1025–39

Gónzalez-Soto X, Expósito M R, Sánchez-Nieto B, Amgarou K, Lagares J I, Gómez F, Domingo C and Sánchez-Doblado F 2012 Neutron spectra inside an adult and children anthropomorphic phantoms in high energy radiotherapy *Proc. IFMBE World Congr.* **39** 1145–48

Hendricks J S *et al* 2008 Monte Carlo N-Particle Transport Code System for Multiparticle and High Energy Applications, Version 2.6.0, Los Alamos National Laboratory

ICRP 2003 *Relative Biological Effectiveness (RBE), Quality Factor (Q), and Radiation Weighting Factor (w_R)* (ICRP Publication 92) (Oxford: Pergamon)

ICRP 2007 *The 2007 Recommendations of the International Commission on Radiological Protection* (ICRP Publication 103) (Amsterdam: Elsevier)

ICRU 1998 Conversion coefficients for use in radiological protection against external radiation ICRU Publication 57

ISO 1998 Neutron reference radiations—Part 3: Calibration of area and personal dosemeters and determination of their response as a function of neutron energy and angle of incidence ISO Standard 8529-3

ISO 2000 Reference neutron radiations—Characteristics and methods of production of simulated workplace neutron fields ISO Standard 12789

Jiménez-Ortega E, Expósito M R, González-Soto X, Terrón J A, Gómez F and Sánchez-Doblado F 2011 Characterization of the neutron induced single event upset in SRAM around high megavoltage clinical accelerators *12th European Conf. Radiation and Its Effects on Components and Systems (RADECS)* pp 922–5

Kluge H, Alevra A V, Jetzke S, Knauf K, Matzke M, Weise K and Wittstock J 1997 Scattered neutron reference fields produced by radionuclide sources *Radiat. Prot. Dosim.* **70** 327–30

Kry S F, Salehpour M, Followill D S, Stovall M, Kuban D A, White R A and Rosen I I 2005 Out-of-field photon and neutron dose equivalents from step-and-shoot intensity-modulated radiation therapy *Int. J. Radiat. Oncol. Biol. Phys.* **62** 1204–16

Leal A, Sánchez-Doblado F, Perucha M, Carrasco E, Rincón M, Arráns R and Bernal C 2004 Monte Carlo simulation of complex radiotherapy treatments *Comput. Sci. Eng.* **6** 60–68

Muñiz J L, Alves J G and Delgado A 1999 Detection and determination limits using glow curve analysis for LiF:Mg,Ti and LiF:Mg,Cu,P based Tl dosimetry *Radiat. Prot. Dosim.* **85** 57–61

Muñiz J L, Vicente M C, González E M, Romero A M, Embid M and Delgado A 2004 A new area multidetector dosemeter for mixed n-γ fields *Radiat. Prot. Dosim.* **110** 243–8

Pena J, Franco L, Gómez F, Iglesias A, Pardo J and Pombar M 2005 Monte Carlo study of Siemens PRIMUS photoneutron production *Phys. Med. Biol.* **50** 5921–33

Siebert B R L and Schuhmacher H 1995 Quality factors, ambient and personal dose equivalent for neutrons, based on the new ICRU stopping power data for protons and alpha particles *Radiat. Prot. Dosim.* **58** 177–83

Thomas D J and Alevra A V 2002 Bonner sphere spectrometers—a critical review *Nucl. Instrum. Methods Phys. Res.* A **476** 12–20

Xu X G, Bednarz B and Paganetti H 2008 A review of dosimetry studies on external-beam radiation treatment with respect to second cancer induction *Phys. Med. Biol.* **53** R193–241